

Damian Crosby¹
 Lutong Li
 Andrew Weightman

Department of Mechanical and Aerospace Engineering,
 School of Engineering,
 Faculty of Science and Engineering,
 The University of Manchester,
 Manchester,
 United Kingdom
 email: damian.crosby@manchester.ac.uk

Joaquin Carrasco
 William Heath
 Department of Electrical or Electronic Engineering,
 School of Engineering,
 Faculty of Science and Engineering,
 The University of Manchester,
 Manchester,
 United Kingdom

Design and Evolution of a Triad Twisted String Actuator for Controlling a Two Degrees of Freedom Joint: Improving Performance and Investigating Active Transmission Adjustment

Actuated universal joints are used in a wide range of robotic applications, including mobile snake robots, snake-arm robots and robotic tails. Depending on the application and design constraints, these can use remote cable or fluid driven systems, or inline motors. In order to realise the benefits of inline actuation while keeping the system compact with a high power to weight ratio, an actuated universal joint (AUJ) was developed using an “antagonistic triad” of three twisted string actuators in our previous work. However, the design of this system had numerous drawbacks in its prototype form, namely a limited angle range, poor accuracy due to the angular feedback sensors used, and issues with string failure due to mechanical design choices. In this publication, we identify and address these challenges through design changes, and as a result angle range was increased from $\pm 14.50^\circ$ to $\pm 26.00^\circ$ for a single axis, and $\pm 6.00^\circ$ to $\pm 20.00^\circ$ for a dual axis movement.

Keywords: Flexible Robots, Force Control, Tendon/Wire Mechanism

1 Introduction

Actuated universal joint (AUJ) mechanisms are crucial in various robotic applications like confined space inspection with continuum robots, highly manoeuvrable snake robots, and biomimetic robot tails for stability. These mechanisms can either use inline actuators, which directly move the joint [1–3], or cable/fluid driven systems relying on a static “base” to house actuators or compressors [4]. Inline actuators necessitate high torque due to lifting the mass of subsequent sections, while systems with a static base require additional space, limiting their utility in mobile robots.

First developed by (author?) [5], the twisted string actuator (TSA) uses two or more strings between two fixtures as a linear actuator. Rotating one fixture, typically with an electric motor, twists the strings into a helix, decreasing the distance between them, as shown in figure 1. Given the unwound length l_u in meters, and the cross-section radius of the string r_s (or $r_s + r_c$ when there are more than two strings, where r_c is the radius of a tangentially constrained circle drawn between the strings) in meters as shown in figure 2. The actuator length in meters is given by

$$l_s(\theta_s) = \sqrt{l_u^2 - \theta_s^2 r_s^2}, \quad (1)$$

where θ_s is the motor angle in radians. TSA actuators have applications in hand orthoses, elbow joints, foldable robot arms, and more [6–8].

Alternative electric actuation systems, like leadscrews, require additional gearing for significant reduction increases, which results in larger and heavier actuators. In contrast, a TSA can achieve reduction increases by reducing string thickness or count, thus slightly reducing actuator mass [9]. While leadscrews can marginally increase reduction by decreasing thread lead [10], this

$$\theta_s = 0 \quad \theta_s = 2\pi \quad \theta_s = 20\pi$$

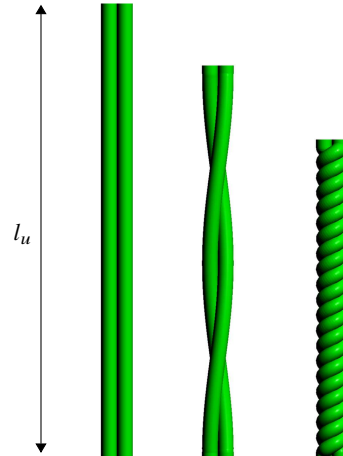


Fig. 1 The value of θ_s increases the number of twists in a string bundle with a string length l_u .

approach faces challenges related to manufacturing tolerances and material limitations. Increasing screw radius also enlarges actuator size and mass similarly. Therefore, from a mechanical perspective, TSA holds an advantage over leadscrews by increasing reduction without adding mass.

One of TSAs main challenges is its reduction variation with motor angle, exhibiting an inverse nonlinear relationship [5,9]. String compliance under high force conditions also requires consideration, which can be addressed through accurate modeling [11] or a robust control strategy that disregards compliance in the system

¹Corresponding Author.
 March 12, 2025

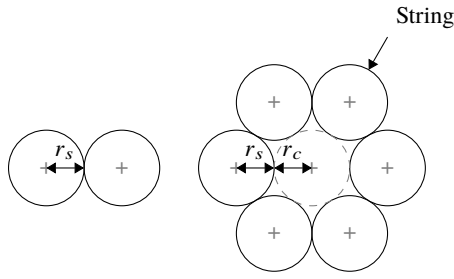


Fig. 2 The location of r_s and optionally r_c in a string bundle.

model [5,9]. Since TSA can only apply force in tension due to string flexibility, single DOF TSA actuator joints need a spring return mechanism, limiting actuator range as spring force increases with decreasing maximum TSA force [12]. A linear force return mechanism was developed to partially mitigate this issue, but the ideal solution involves using a second synchronized TSA actuator to achieve a matching antagonistic force profile [7,13–15]. Thus, a 2 DOF actuator can be realized without springs by adding a third TSA.

The use of TSAs as an actuator for AUJs remains an under-studied area of research. (author?) [16] proposed a similar design using a flexible core with continuous curvature instead of a rigid universal joint, presenting an open-loop control solution for multi-axis control using only two TSAs at a time, albeit with a limited azimuthal axis range. In contrast, we demonstrate robust closed-loop control of an AUJ in both axes of motion, covering the full azimuthal range of $[0, 360]^\circ$, using three TSAs in an “antagonistic triad” configuration. This results in a light, compact AUJ design with potential improvements over existing inline actuation options.

Our aim in this publication is to address the issues present in the original design, and analyse and evaluate the performance characteristics and special properties of the TSA antagonistic triad mechanism, in order to prepare it for implementation in a future practical application. As such, we extended our work in [17] by identifying shortcomings in the original prototype (hereafter referred to as such) and addressing them through design changes to create an “improved prototype” (hereafter referred to as such). We also conducted additional experiments to further characterise the mechanism, by examining the effect of additional follower mass and increased joint velocity. Finally, we have looked at existing snake robots in literature, and have compared how a theoretical robot with this mechanism would compare in terms of performance, specifically the self-supporting segment limit. The main contributions of this work are as follows:

- Identification of improvements that could be made to the original prototype through design changes, and experimental results detailing the performance improvements realised as a consequence.
- Additional experiments conducted to further characterise the performance of the AUJ by the addition of additional mass to the follower and increasing joint velocity.
- A simulation of active transmission adjustment (ATA) which allows the mechanism to change specific performance characteristics in real time during operation.
- Analysis of a theoretical multi-segment antagonistic triad TSA design against existing snake robots.

In section 2 we give a brief summary of the design of the original prototype, in order to furnish the reader with enough information to understand the rest of the publication. More information can be found in [17]. In section 3 we identify each improvement we address through design alterations, explain the alterations made,

and show the results that demonstrate the improved performance. In section 4 we show the results of additional experiments to further characterise the mechanism. In section 5 we discuss the remaining limitations of the improved prototype, the ATA simulation, and a distributed control proposal for multi-segment operation. We also compare a theoretical multi-segment design to other snake robots in this section. Finally, section 6 then summarises the publication and discusses future work.

2 Original Prototype Design Summary

Because TSA can only operate in tension, a minimum of three TSA are required to operate an AUJ. These can be arranged into an “Antagonistic Triad” where adjusting the length of each TSA changes the orientation of the AUJ, in a similar fashion to other cable driven robotic systems [4]. These lengths can be combined into a vector function

$$\begin{aligned} \lambda_1(\theta) &= \sqrt{a + 2l_1r \sin(\theta_2) \cos(\theta_1) + l_2^2} \\ &\quad + 2l_2r \sin(\theta_2) - 2r^2 \cos(\theta_2) + 2r^2 \\ \lambda_2(\theta) &= \sqrt{a + b + c - d} \\ \lambda_3(\theta) &= \sqrt{a - b - c + d} \\ \text{where: } & \\ a &= l_1^2 + 2l_1l_2 \cos(\theta_1) \cos(\theta_2) \\ b &= \sqrt{3}l_1r \sin(\theta_1) - l_1r \sin(\theta_2) \cos(\theta_1) + l_2^2 \\ c &= \sqrt{3}l_2r \sin(\theta_1) \cos(\theta_2) - l_2r \sin(\theta_2) \\ d &= \frac{\sqrt{3}r^2 \sin(\theta_1) \sin(\theta_2)}{2} - \frac{3r^2 \cos(\theta_1)}{2} - \frac{r^2 \cos(\theta_2)}{2} + 2r^2, \end{aligned} \tag{2}$$

where $\Lambda(\theta) = [\lambda_1(\theta) \quad \lambda_2(\theta) \quad \lambda_3(\theta)]$ is a vector function which outputs the magnitudes of each point pair, and therefore the lengths of each actuator, assuming both ends of each actuator can rotate freely on both x and y axes. Other coefficients are labelled in figure 3.

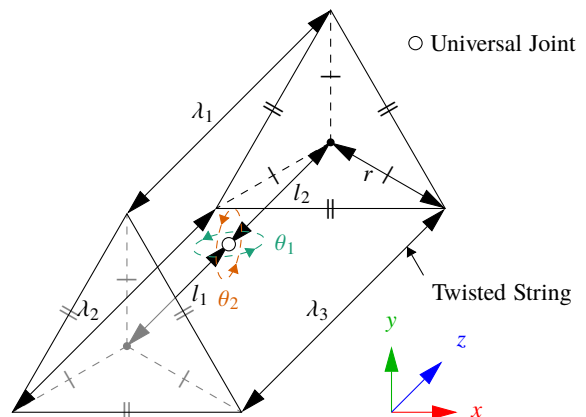


Fig. 3 Kinematic diagram of the antagonistic triad, where the universal joint rotation is defined by $\theta_{1,2}$ on the y and x axes respectively, and the actuator lengths are defined by $\lambda_{1,2,3}$ for the top, left and right strings, and r and $l_{1,2}$ define the anchor points of the strings.

After an investigation into a position based kinematic control system in the original prototype proved unsuccessful, a force based

control system was developed, which uses the inverse dynamics of the AUJ to convert angular velocity from a PID controller into angular torque, which is then turned into force setpoints for each TSA using an optimising algorithm based on [18]. The control system is a four layer cascade design, joining an outer loop PID controller C_1 to an inverse dynamic control system C_2 [19], to the triad force controller C_3 in [18], to a proportional controller C_4 for each TSA. It uses feedback signals of the joint position and TSA force.

C_3 uses the *inverse force transformation* algorithm from [18] with the jacobian of (2) to select an optimal force vector from the desired joint torque. Here it is presented in an unexpanded and more general form,

$$J_\Lambda = \begin{bmatrix} \frac{\partial \lambda_1}{\partial \theta_1} & \frac{\partial \lambda_2}{\partial \theta_1} & \frac{\partial \lambda_3}{\partial \theta_1} \\ \frac{\partial \lambda_1}{\partial \theta_2} & \frac{\partial \lambda_2}{\partial \theta_2} & \frac{\partial \lambda_3}{\partial \theta_2} \end{bmatrix}$$

$$\gamma(i) = -J_{\Lambda_{-i,*}}^{-T} (J_{\Lambda_{i,*}}^T f_{min} + \tau) \quad (3)$$

$$F(\tau, \theta) = \begin{bmatrix} f_{min} & \gamma(2)_1 & \gamma(3)_1 \\ \gamma(1)_1 & f_{min} & \gamma(3)_2 \\ \gamma(1)_2 & \gamma(2)_2 & f_{min} \end{bmatrix}.$$

A force matrix F is created from the torque input τ , jacobian J_Λ from the vector function Λ as defined in equation 2, and minimum force constant f_{min} . f_{ii} is equal to f_{min} , while the other elements in the column are based on a calculation using $J_{\Lambda_{-i,*}}$ where $-i$ is a row removed from the matrix. Algorithm 1 is then used to create output force vector f , which minimises the net force on all TSA while producing the desired output torque on the universal joint.

Algorithm 1 Selects one column of F to be the output force vector f , where \top and \perp are boolean *true* and *false* respectively, and $f_{*,i}$ is the i th column of F .

```

1:  $s \leftarrow [\top \top \top]$ 
2: if  $f_{23} > f_{min}$  then  $s_2 \leftarrow \perp$  else  $s_3 \leftarrow \perp$  end if
3: if  $f_{31} > f_{min}$  then  $s_3 \leftarrow \perp$  else  $s_1 \leftarrow \perp$  end if
4: if  $f_{12} \geq f_{min}$  then  $s_1 \leftarrow \perp$  else  $s_2 \leftarrow \perp$  end if
5: for  $i = 1$  to  $3$  do
6:   if  $s_i \rightarrow \top$  then  $f_{set} \leftarrow f_{*,i}$  end if
7: end for
```

Figure 4 shows a complete block diagram of the control system.

2.1 Original Prototype Limitations. After the experiments were conducted on the original prototype in [17], several shortcomings with the design were noted that reduced the performance of the system:

- **Limited AUJ Angle Range** - The AUJ angle tracking experiments in [17] only had a range of $\pm 14.50^\circ$ in a single axis, and $\pm 6.00^\circ$ for both axes. This was because one or more TSA would completely “unwind” near that limit and be unable to lengthen further. This limits the practicality of such a mechanism, for example a multi-segment design would have a very large minimum curvature. Increasing f_{min} does increase the angle range marginally by increasing the TSA motor angle at $\theta = [0 \ 0]^\top$, which was proven experimentally, as shown by experiments conducted on the original prototype in figure 5. These experiments were able to achieve modest increases of $4.00^\circ \text{ N}^{-1}$ for the positive (upper) limit of the universal joint roll θ_1 , and $-6.06^\circ \text{ N}^{-1}$ for the negative (lower) limit, within the f_{min} interval [3, 3.5]. However, further attempts to increase f_{min} , or attempts to perform the same experiment on the pitch axis resulted in premature string failure. It was also clear to achieve significant increases in AUJ angle range, a different approach would be needed that would require modifications to the design.

Table 1 Table of the minimum and maximum values of $\Lambda(\theta)$ at different values of r in the interval of $[-\frac{\pi}{2}, \frac{\pi}{2}]$.

r [mm]	$\lambda_1(\theta)$ [mm]		$\lambda_2(\theta)$ [mm]		$\lambda_3(\theta)$ [mm]	
	Min.	Max.	Min.	Max.	Min.	Max.
13.0	42.64	68.35	42.64	68.57	42.64	68.57
10.0	45.02	64.88	45.02	64.98	45.02	64.98
7.25	47.33	61.78	47.33	61.82	47.33	61.82

- **Poor AUJ Angle Measurement Accuracy** - The original prototype used a Bosch Sensortec BNO080 9 degree of freedom (DOF) inertial measurement unit (IMU) [20] to measure the AUJ orientation. The original plan was to use two IMUs, on the base and follower bodies, and the orientation would be calculated from the difference. However, the magnetometer measurements proved to be unreliable inside the laboratory, so only a single IMU was used and the base segment was orientated with the gravity vector parallel to the z axis. due to inconsistent magnetometer readings inside the laboratory, only one IMU was implemented, aligning the base body with gravity along the z axis. This allowed the AUJ orientation to be calculated from only the accelerometer readings, but meant the mechanism could only be controlled when orientated in the vertical axis. There was also an issue with the IMU resolution, which was only accurate to within $\pm 1.50^\circ$ [20]. A Savitsky-Golay filter was applied to the results in [17] for data presentation purposes and to more accurately represent the true AUJ angles at that point in time.

Also, to enable the mechanism to be controlled in any direction relative to gravity, a solution that can directly measure the mechanical angular displacement of the universal joint was required.

- **String Failures** - One reoccurring issue was the TSA strings breaking at high values of θ_s , which became more common after a number of twisting and untwisting cycles. Occasionally this was caused by a failure of limit monitoring within the control system ($f > 9$), but failure would also occur within normal operating conditions ($f \leq 9$).

3 Methodology

3.1 Original Prototype Improvements.

3.1.1 Increasing AUJ Angle Range. The most effective modification to improve AUJ angle range is to reduce the value of r in (2). This decreases the stroke length required for each TSA to achieve the same AUJ angle range as shown by table 1, which also reduces the TSA motor angle accordingly, allowing a greater AUJ angle to be reached before one or more TSA unwind. This can be done by using smaller motors, or by using the same size or larger motors with offset shafts connected by spur gears. Smaller motors were chosen, with a cross section of only 120.00 mm^2 compared to 227.00 mm^2 on the existing design. These were Guangdong Kingly Gear Co. Micro Metal Gearmotors (50:1) [21], were lighter than the existing motors, 18.00 g compared to 27.00 g , and the mechanism would be less complex. These motors have a much lower θ_{max} than the existing motors of only 44.00 rad s^{-1} compared to $442.00 \text{ rad s}^{-1}$ [22], but since the original experiments limited the motor velocity to 10.00 rad s^{-1} to ensure mechanism stability, this is not a concern. This change of motors allowed r to be reduced from 13.00 mm to 7.25 mm .

To achieve this reduction, additional design changes were necessary. The close proximity of the TSA strings made a central shaft impractical, unlike in the original prototype. Instead, a “hollow spider” arrangement was adopted for the universal joint, allowing the TSA strings to pass through its center, as shown in Figure 6.

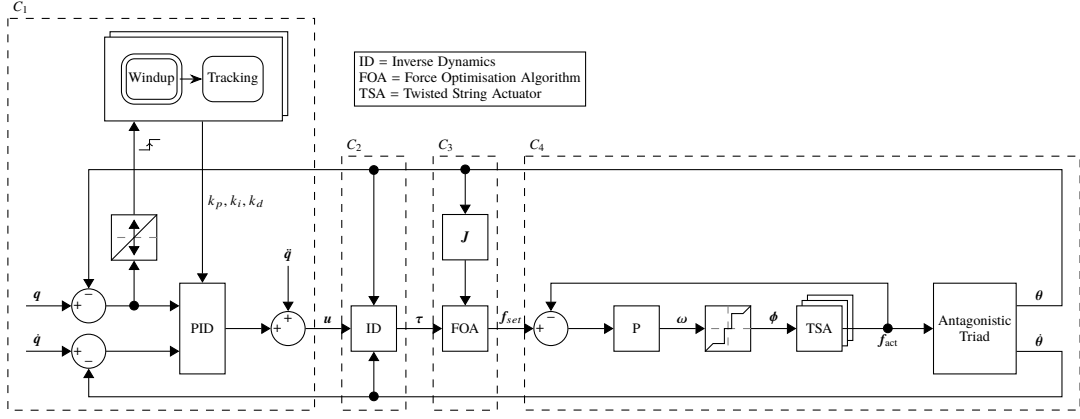


Fig. 4 Block diagram of the complete experimental control system, excluding the hardware velocity controllers for the motors. Dashed boxes correspond to the control layers $C_{1\ldots 4}$.

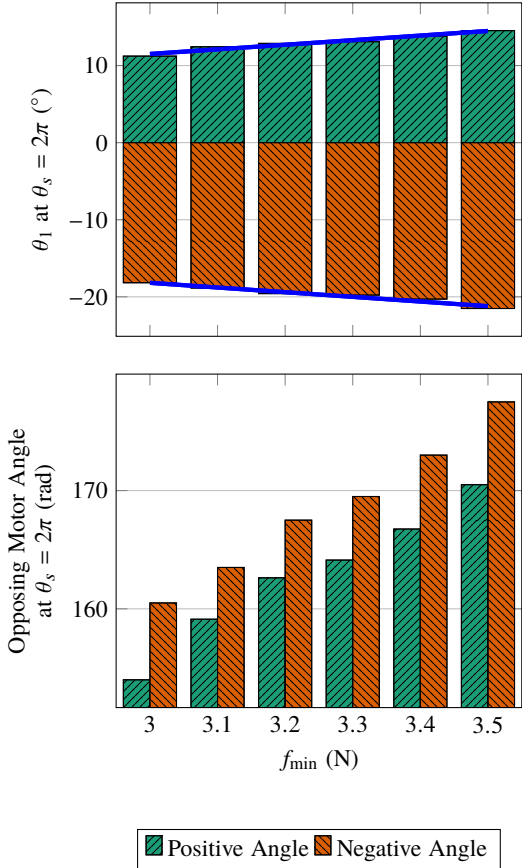


Fig. 5 AUJ roll angle (θ_1) of the original prototype when the smallest TSA motor angle is equal to 2π , and motor angle of the “opposing” TSA (the TSA with the largest motor angle) at the same position.

This modification also provided space for directly installing AUJ angle sensors onto the universal joint, as detailed in Section 3.1.2.

3.1.2 Improving AUJ Angle Measurement Accuracy. Two options were considered to address this issue: potentiometers and hall effect sensors. A potentiometer would link each universal joint spider axis to a resistive track, altering its resistance based on AUJ orientation and providing an analog voltage signal to the controller. Mechanical stops would ensure the required AUJ angle range could

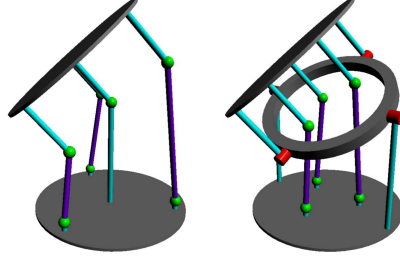


Fig. 6 An AUJ with a central universal joint, and one with a hollow spider. The hollow spider allows r to be decreased as space is no longer required for a central universal joint.

be measured during assembly. Alternatively, a hall effect sensor would use a radially bipolar magnet on the shaft's end with a hall effect sensor beneath it, providing analog voltage signal or digital data for the axial orientation of the magnet and, consequently, the shaft [23]. The potentiometer solution, chosen for its simplicity of control integration and integrated mechanical stops, would be simpler to integrate into the existing control system, requiring only an analog to digital converter (ADC) and a slope-intercept form for conversion to an AUJ angle. The Bourns PDB08, selected for its small size and internally threaded shaft, was chosen as the potentiometer [24]. Operating as a voltage divider at +5.00 V, the PDB08 would offer a resolution of approximately $40.00^\circ \text{ V}^{-1}$. With the 12-bit resolution of the onboard ADC for myRIO analog inputs, this yields a theoretical resolution of approximately 0.05° compared to $\pm 1.50^\circ$ for the BNO080. The potentiometer's sliding noise (maximum 100.00 mV) would reduce this during AUJ motion, partially mitigated with filtering. This improvement from the IMU was deemed significant enough for use in the latest prototype, validated through experimental testing, rendering further investigation of the hall effect sensor unnecessary.

3.1.3 Preventing String Failure. Analysis of the design revealed “pinch points” and “bite points”, where the string could deform or weaken due to contact with surfaces or sharp edges, as depicted in figure 7(a). Removing these points by rounding off edges and using alternative string securing methods, such as tying it into a loop instead of using grub screws, eliminated potential sources of string damage, as shown in figure 7(b). However, nylon monofilament, like the TSA string, is still prone to torsion fatigue, reducing its tensile strength. To address this, the SeaKnight BLADE 0.20 mm nylon monofilament was replaced with 0.20 mm Dyneema® polyfilament string, as used in [9]. Design changes to the string clamp facilitated easier installation of the polyfilament string, making it a practical option.

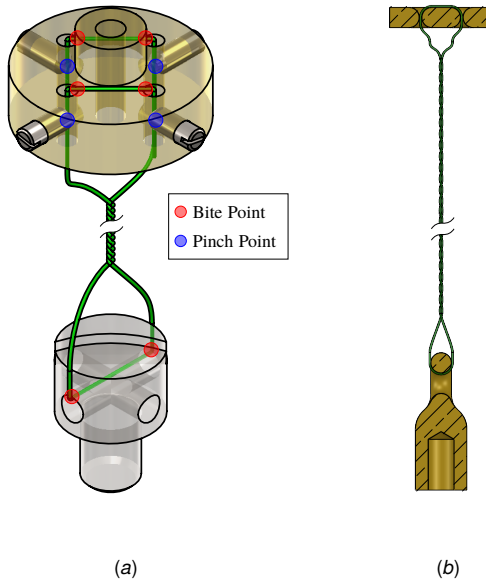


Fig. 7 (a) The original TSA string loop between the string clamp and capstan bolt, with “pinch” and “bite” points indicated, where premature string failure may occur. (b) Section view of the new TSA string loop showing how the pinch and bite points have been eliminated.

Table 2 Model coefficients for the latest prototype.

Coeff.	Value	Coeff.	Value
l_1	55.00 mm	f_{min}	3.00 N
l_2	0.00 mm	r_s	200.00 μm
r	7.25 mm	m	61.60 g
l_u	55.00 mm	$\dot{\theta}_{s_{max}}$	44.00 rad s^{-1}
τ_{\max}	0.04 N m	ρ	[0.00 0.00 3.05] mm

Coeff.	Value
I	$\begin{bmatrix} 2.80 \times 10^{-5} & 0.00 & 0.00 \\ 0.00 & 2.60 \times 10^{-5} & 0.00 \\ 0.00 & 0.00 & 5.00 \times 10^{-6} \end{bmatrix} \text{kg m}^{-2}$

3.1.4 Final Design of Improved Prototype. Figure 8 presents an annotated schematic of the improved prototype, and figure 9 shows a photograph with the AUJ axes annotated. The load cells remained unchanged from the original prototype, while alterations were made to the universal joints below them. The hollow spider was connected to the base and follower bodies using machine precision bearings and bushings to ensure smooth motion. Regarding the control system, the Faulhaber MCDC3002 motor controllers [25] were replaced with a single Pimoroni Motor 2040, capable of handling up to four Micro Metal Gearsmotors with Micro Metal Motor Encoders attached. Programming was done with a velocity controller similar to the one provided in the pimoroni-pico library. Furthermore, the deadband compensation threshold was reduced to $\pm 0.50 \text{ rad s}^{-1}$ due to the smaller deadband region of the motors, while the motor velocity limit of 10.00 rad s^{-1} remained unchanged.

3.2 Experimental Comparison of Improved Prototype to Original Prototype. In order to validate and quantify the efficacy of the improvements we made, we conducted two experiments, one to measure the increase in AUJ angle range and another to measure the AUJ angle measurement accuracy. We also did not observe any string failure during normal operation ($f \leq 9$), which demonstrated the efficacy of the improvements made to address that

Table 3 PID gains used for the experiment.

Gain	Value	
	Windup	Tracking
k_p	2.00×10^5	8.00×10^5
k_i	3500.00	3500.00
k_d	0.00	50.00
k_{ps}	5.00	5.00

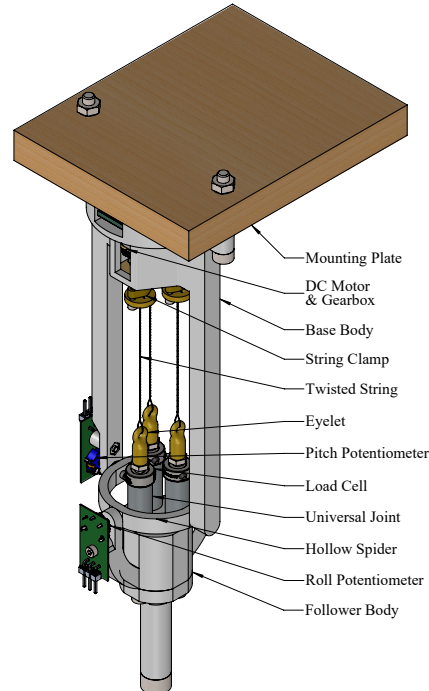


Fig. 8 Schematic of the latest prototype with labelled components.

issue. Table 4 shows a summary of the effects of our improvements to the mechanism.

3.2.1 AUJ Angle Range. To evaluate the expanded AUJ angle range, we replicated the setpoint tracking experiments from [17]. Figure 10 illustrates the tracking response in both the pitch and roll axes. Mechanical limitations restricted the AUJ angle range to $\pm 26.00^\circ$. This constraint resulted from the hollow spider colliding with the TSA universal joints in the pitch axis and with the follower body in the roll axis. For the dual-axis trajectory, the angle range was further constrained to $\pm 20.00^\circ$ due to a load cell exceeding a safety limit of 9.00 N (with the load cell full scale being 9.80 N [26]).

3.2.2 AUJ Angle Measurement Accuracy. Figure 11 shows the difference between the BNO080 IMU and PDB08 potentiometer when the AUJ is at rest. The minimum measured change in value was 0.21° for the BNO080 and 0.11° for the PDB08, a significant increase in measured accuracy.

4 Additional Experimental Results

4.1 The Effect of Follower Mass on AUJ Angle Tracking. For a multi-segment design, analyzing the AUJ performance with a non-negligible follower mass is crucial. This addition alters the system dynamics, affecting the inverse dynamic calculations in the

Table 4 Summary of all the performance improvements and the measurements used to quantify them.

Improvement	Measurement	Results	
		Original	Improved
Increasing AUJ angle range	Maximum AUJ angle	14.50°	26.00°
Improving AUJ angle measurement accuracy	Minimum step change in AUJ angle measurement.	0.21°	0.10°
Preventing string failure	String failed when $f \leq 9\%$	✓	✗

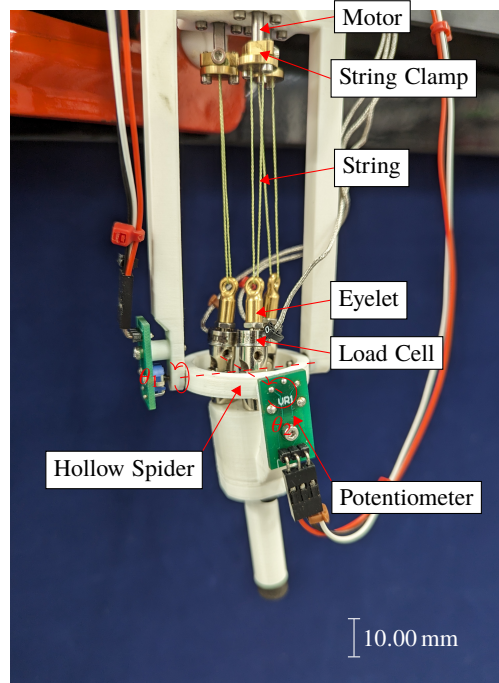


Fig. 9 Annotated photograph of the single segment physical prototype antagonistic triad, with the roll θ_1 and pitch θ_2 axes marked.

Table 5 Table of all the follower mass configurations, with the parameters for follower mass m and follower COM z offset ρ_3 .

Config.	m [g]	ρ_3 [mm]	I [kg m ⁻²]	Image
No Mass	61.60	3.05	diag $\begin{pmatrix} 2.80 \times 10^{-5} \\ 2.60 \times 10^{-5} \\ 5.00 \times 10^{-6} \end{pmatrix}^\top$	
+20 g	81.29	15.74	diag $\begin{pmatrix} 6.90 \times 10^{-5} \\ 6.80 \times 10^{-5} \\ 7.00 \times 10^{-6} \end{pmatrix}^\top$	
+50 g	111.10	26.39	diag $\begin{pmatrix} 1.06 \times 10^{-4} \\ 1.05 \times 10^{-4} \\ 1.10 \times 10^{-5} \end{pmatrix}^\top$	
+80 g	140.35	32.44	diag $\begin{pmatrix} 1.29 \times 10^{-4} \\ 1.27 \times 10^{-4} \\ 1.20 \times 10^{-5} \end{pmatrix}^\top$	

Table 6 Trapezoidal trajectory sequence parameters.

Cycle	Max./Min. Angle [rad]	Max. Velocity [rad s ⁻¹]	Acceleration [rad s ⁻²]
1	0.40	0.40	1.00×10^{-2}
2	0.40	0.44	1.10×10^{-2}
3	0.40	0.48	1.21×10^{-2}
4	0.40	0.53	1.33×10^{-2}

control system, as illustrated in table 5. In figure 12, the response for a roll trajectory with varying follower body masses (20.00 g, 50.00 g, and 80.00 g) is depicted. Due to load cell safety limit of 9.00 N, larger masses could not be tested. Initially, setting k_p to the value in table 2 failed to achieve a steady state except for the “No Mass” configuration. By reducing k_p to 8000 in weighted configurations, a steady state was achieved with a maximum tracking error of 0.85°, similar to initial experiments. However, for the “No Mass” configuration, setting k_p to 8000 resulted in a poor tracking error of 3.06°, contrasting with the 0.76° maximum tracking error obtained with k_p from table 2. In future implementations, gain scheduling could optimize k_p selection for a given follower mass, minimizing tracking error while ensuring a steady state.

4.2 The Effect of AUJ Angular Velocity on AUJ Angle Tracking. To assess the AUJ performance at higher angular velocities, we repeated the experiments from section 3.2.1, but for each single axis. Using a trapezoidal “chirp” signal, we reduced the angle range to $\pm 23.00^\circ$ to prevent overshoot. Each cycle increased the maximum angular velocity by $\omega_0 + (2(n-1)\omega_0)$ and the angular acceleration by $\alpha_0 + (16(n-1)\alpha_0)$, where n is the cycle number and ω_0 and α_0 are initial values. Four cycles were executed, with the maximum velocity and acceleration values detailed in table 6. Figure 13 displays the experiment results, demonstrating a slight increase in tracking error with rising maximum angular velocity and acceleration. However, the pitch experiment could not be completed due to the load cell force exceeding the safety limit of 9.00 N, as evident in the figure.

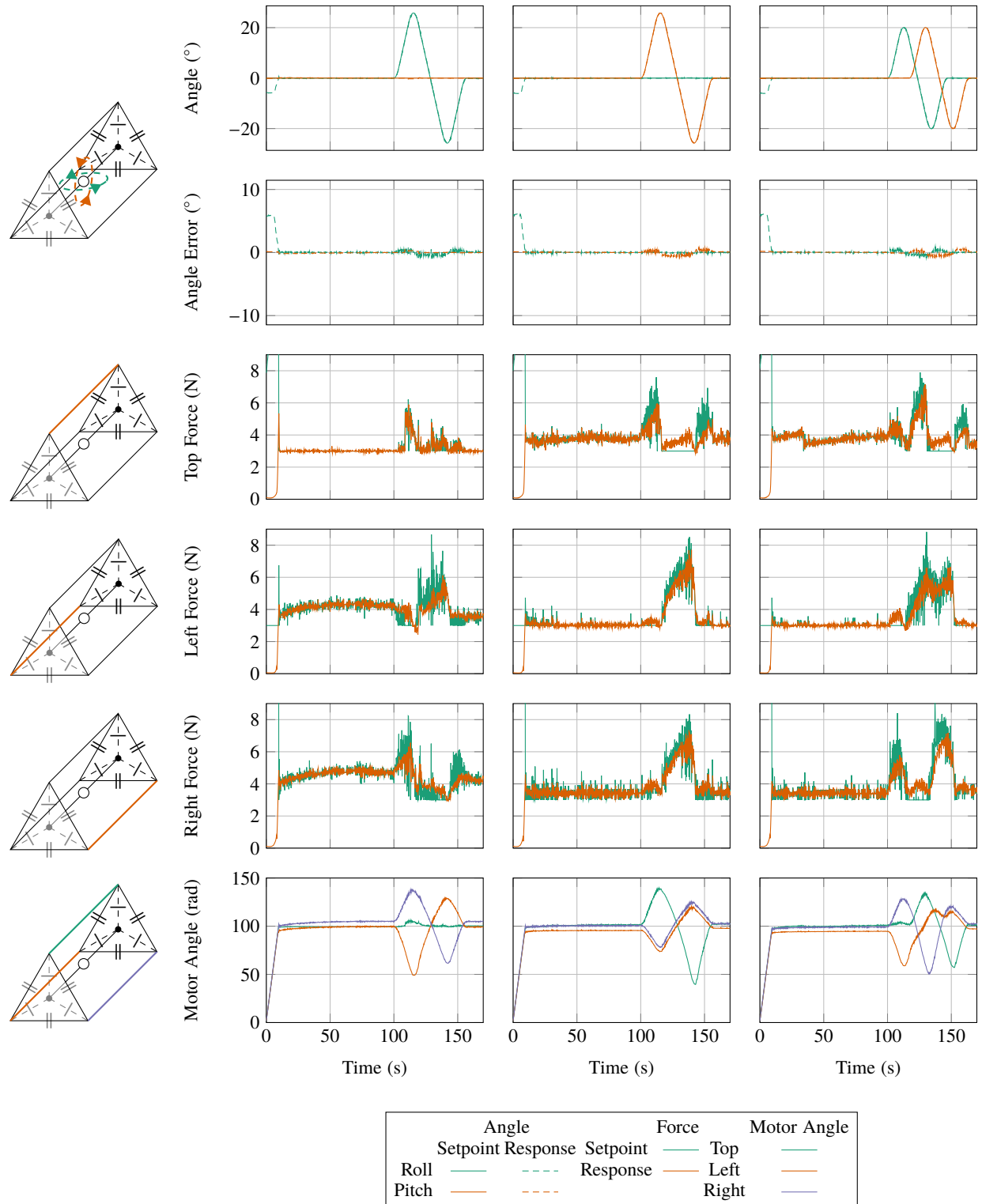


Fig. 10 Plots of the response for three different trajectories, one on only the roll axis θ_1 (column 1), one on only the pitch axis θ_2 (column 2), and one on both axes θ_1 and θ_2 (column 3). Plots include AUJ orientation, forces at the top, left and right TSA, and the motor positions.

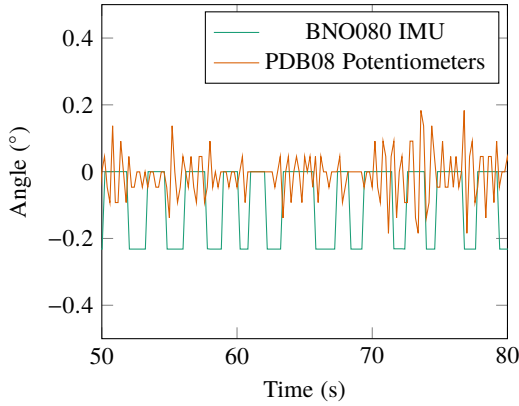


Fig. 11 Comparison of the roll (θ_1) angle signal from the BNO080 IMU and PDB08 potentiometer when the AUJ is at rest at setpoint $\theta = [0 \ 0]$.

5 Discussion

5.1 Active Transmission Adjustment (ATA). The TSA mechanism exhibits a non-linear transmission ratio dependent on θ_s (see Figure 14). This leads to an inverse relationship between the maximum stroke velocity \dot{p}_{\max} and maximum tensile force f_{\max} as θ_s increases. Using the jacobian from [11], f_{\max} and \dot{p}_{\max} are found as

$$\begin{aligned} \mathcal{J} &= \frac{\theta_s r_s^2}{l_u - p} \\ \mathcal{J}^{-1} &= \frac{l_u - p}{\theta_s r_s^2} \\ f_{\max} &= \mathcal{J}^{-1} \tau_{\max} \\ \dot{p}_{\max} &= \mathcal{J} \dot{\theta}_s \tau_{\max}. \end{aligned} \quad (4)$$

Thus, increasing θ_s decreases f_{\max} and increases \dot{p}_{\max} for the same stroke p , with a greater effect if p increases. Adjusting f_{\min} requires increasing the minimum value of θ_s for each TSA. This real-time alteration of f_{\min} can modify TSA and AUJ performance during operation, allowing for maximum joint torque to be increased at the expense of joint velocity, or vice versa.

It may be noticed that $\lim_{\theta_s \rightarrow 0} f_{\max} = \infty$, which is a consequence of assuming infinite material stiffness for the strings, which is not possible outside simulation. This poses a challenge for real-world high force applications, as discussed in [11].

With the simulation of the mechanism used in [17] using the AUJ trajectory from figure 10, a parameter sweep of $f_{\min} = \{3.00, 4.00, 5.00, 6.00, 7.00, 8.00\}$ shows the expected increase in total motor torque $\sum_{i=1}^3 \tau_i(t)$ and total TSA force $\sum_{i=1}^3 f_i(t)$ for increasing values of f_{\min} , as shown in figure 15. Attempts were made to verify this experimentally with a modified parameter sweep to stay within load cell limits, however due to motor properties like gearbox backlash and PWM control nature, it was not possible to determine this relationship as the motor torque could not be measured accurately. Future work could explore better analysis methods or consider using brushless DC motors to enable experimental validation.

5.2 Dynamics Gravity Vector. In the experiments, g was assumed parallel to the z axis ($[0 \ 0 \ -9.81]$) due to the vertical orientation of the mechanism. To function in other orientations, an IMU would be necessary to compute the gravity vector, incorporating gyroscopes to counter motion-generated forces.

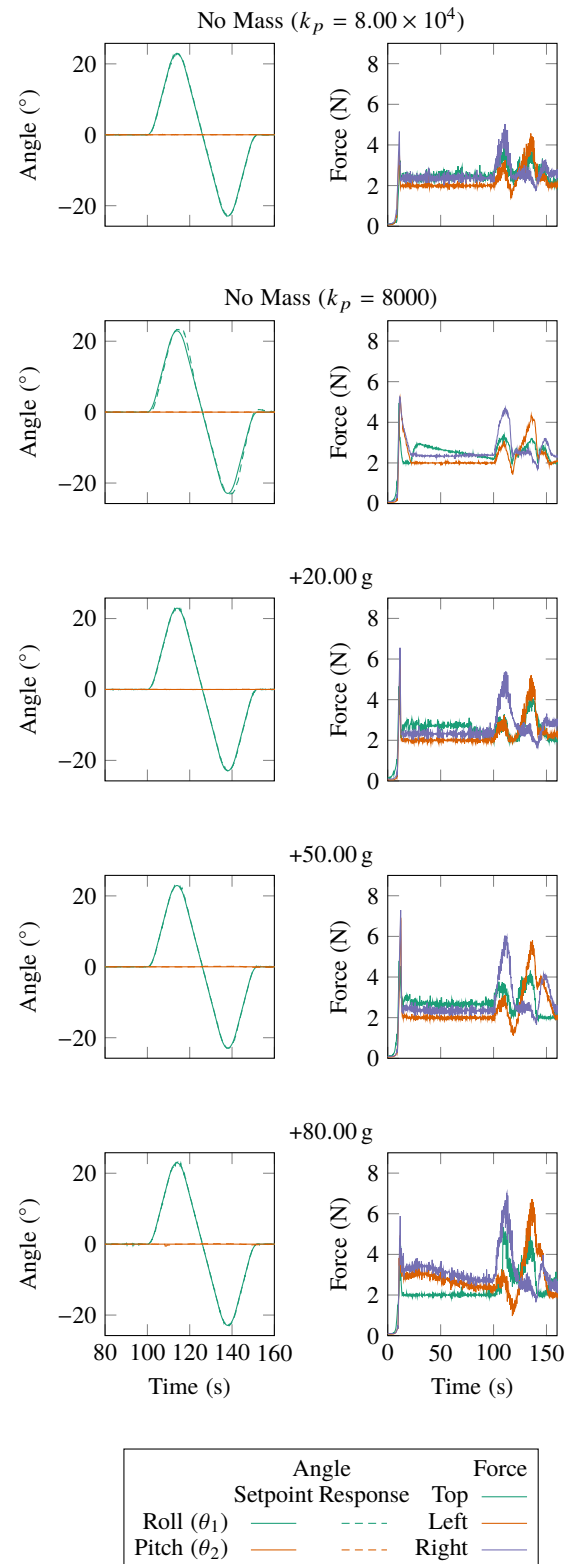


Fig. 12 AUJ roll tracking with increasing follower mass from table 5, plus with no mass at $k_p = 8000$ and $k_p = 8.00 \times 10^4$.

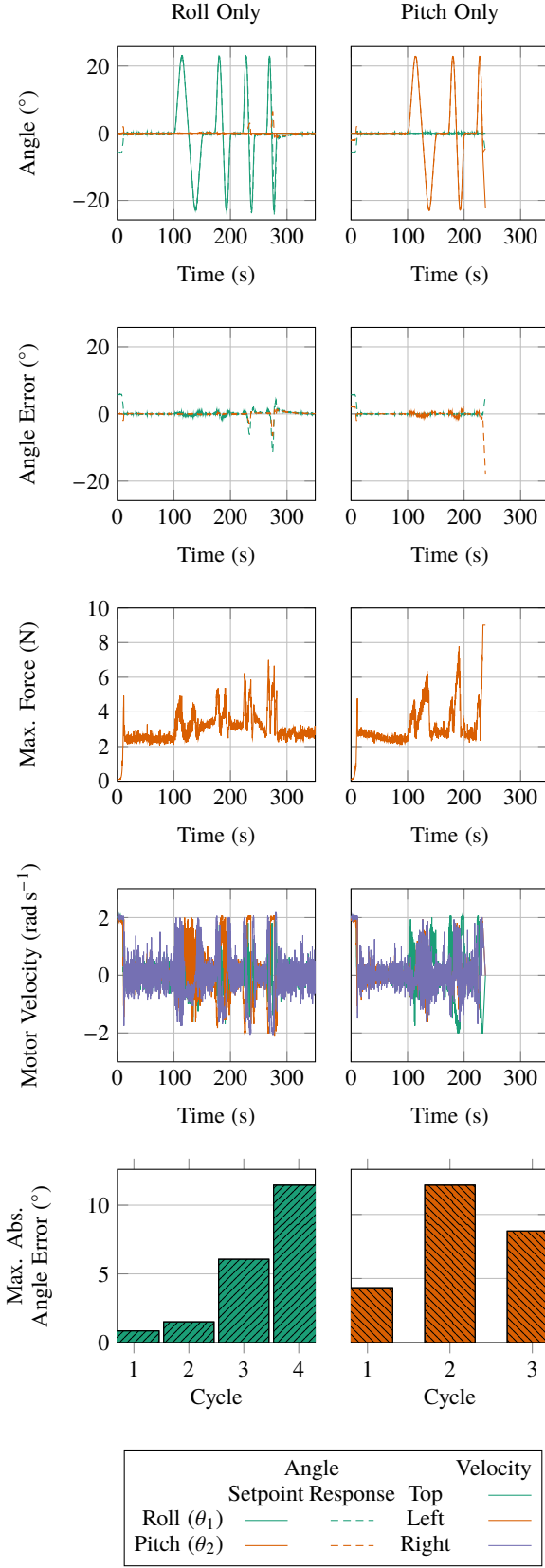


Fig. 13 Results of the trapezoidal velocity trajectory from table 6 for both AUJ pitch and roll trajectories, including the maximum absolute angle error for each cycle.

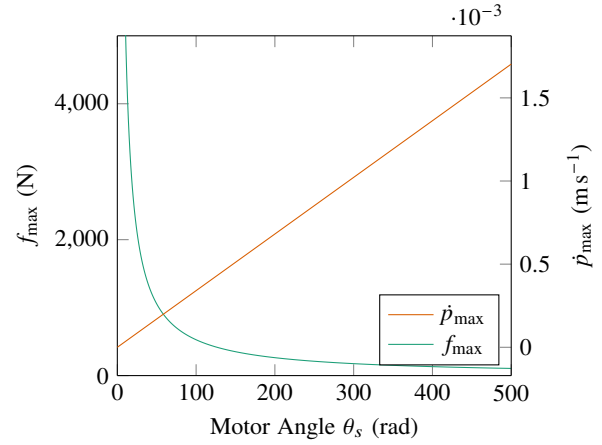


Fig. 14 By adjusting f_{\min} , the transmission ratio of the TSA can be altered. Reducing f_{\min} increases the maximum TSA force f_{\max} while reducing the maximum TSA stroke velocity \dot{p}_{\max} . Conversely, increasing f_{\min} reduces f_{\max} and increases \dot{p}_{\max} . This can be used to actively modify the dynamic properties of the AUJ during operation. In this graph, $\rho = 0$.

5.3 Load Cell Limitation. As noted in sections 3.2.1, 4.1 and 4.2, the load on each TSA being limited to 9.00 N meant that the AUJ angle range was limited with an increased follower mass, increased velocity, and in dual axis operation. Using load cells with a larger full scale would increase the AUJ angle range in all cases.

5.4 Multi-Segment Design. One potential practical application of this mechanism is to chain multiple TSA AUJ together to create a flexible robot comprised of multiple segments. Snake and snake-arm robots are common implementations of chains of AUJ where this mechanism could be implemented. Snake robots in particular are a promising application, since the actuators need to be inline unless the snake robot is tethered, and segment mass is an important factor for agility, manoeuvrability and accommodation of batteries and sensor packages.

5.4.1 Self-Supporting Segment Limit. If we consider a multi segment design of an arbitrary identical segments of mass m , length l and center of mass (COM) offset ρ along the z axis, this can be defined as the maximum number of segments in that can be supported with no contact points under the influence of gravity g in any orientation. This is important for snake robots, as it determines how far they can reach when performing certain manoeuvres that require vertical traversal, such as climbing stairs. For snake-arm robots, it effectively is the limit for the number of segments, since all segments are continuously operating with no contact points. This limit $n_{\lim} \in \mathbb{N}$ is defined by

$$\begin{aligned} \tau_{\max} &\geq \sum_{i=0}^{n-1} m(i l + \rho), \\ \tau_{\max} &\geq mg \left(n\rho + \frac{\ln(n-1)}{2} \right), \\ n_{\lim} &= \left| \frac{1}{2} - \frac{\rho - \sqrt{\frac{l^2}{4} - l\rho + \rho^2 + \frac{2l\tau_{\max}}{mg}}}{l} \right|. \end{aligned} \quad (5)$$

which can be generalised to include designs with heterogeneous segments. Calculating τ_{\max} depends on the design of the actuation system. For "direct drive" motor driven systems, it is simply the

maximum rated torque of the motor. For cable or linear actuator driven systems, it is $f_{\max}r$, where f_{\max} is the maximum rated force of the actuator, and r is the radius distance from the actuator to the pivot axis. For TSA actuators, this is extended to $\mathcal{J}^{-1}\tau_{\max}r$, as shown in equation 4.

Table 7 gives a list of snake robots with inline actuators, identical segments, and their self-supporting segments limit. *Uncle Sam* and *SEA Snake* both have 16 segments of alternating 1 DOF joints, each pair of these is considered one segment in this analysis. Segment COM offsets are not provided, so it is assumed to be $\frac{l}{2}$.

We can then construct a theoretical snake robot made of the TSA AUJ segments in this publication, and see how it would compare to existing snake robots. However, since the prototype was constructed of lightweight 3D printed materials which are not designed to be durable, with a mass of only 61.60 g, a direct comparison would not be entirely fair. Therefore, we have considered designs with additional mass, weighing 300.00 g and 900.00 g respectively. Figure 16 shows the limit as θ_s increases, which outperforms all of the robots in table 7 within 150.00 rad, whereas the experiments conducted in section 4 have a maximum motor angle of 139.80 rad, as shown in figure 10. Test There are limitations to this analysis, as it only uses a simple model for the TSA that does not take into account string compliance and friction, therefore physical implementations are not expected to perform as well. Most of the snake robots in table 7 also have a larger joint angle range than the prototype design, which may be useful for some tasks, such as anchoring to a tree. However, it shows that the TSA AUJ mechanism has a lot of potential in developing highly mobile snake robots with a large number of segments that are able to self-support the majority of said segments, which would allow for increased agility in many environments. It also allows for similarly long snake-arm robots with inline actuation.

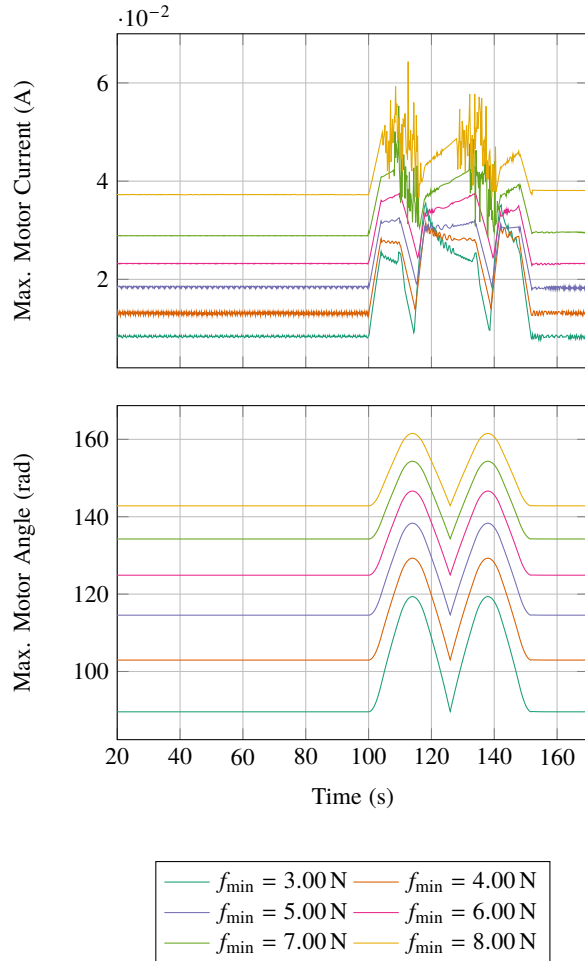


Fig. 15 Sum of TSA maximum motor currents and angles for a simulated roll (θ_1) trajectory from figure 10 at different values of f_{\min} . Simulation uses motor coefficients from Faulhaber 1724TSR motors [22], as motor inertia and friction values are unavailable for Micro Metal Gearmotors.

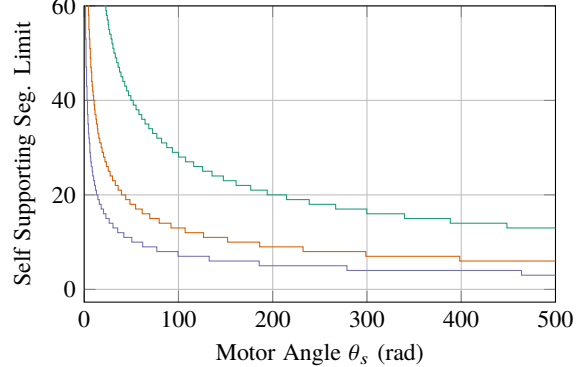


Fig. 16 Graph showing the decrease in self-supporting segments limit as TSA motor angle θ_s increases for different segment masses m at $p = 0$. Segment length is 155.00 mm measured from the prototype, other coefficients as used in figure 14 from table 2.

5.4.2 Distributed Control System. In a multi-segment setup, individual embedded control systems within each segment could receive AUJ angle position setpoints from a central controller. This setup enables the execution of complex trajectories while minimizing wiring complexity through shared power and communication buses, fostering a modular design. Figure 17 shows a conceptual system diagram for this setup.

Table 7 List of snake robots, their number of segments n , their segment mass m , segment length l , maximum joint torque τ_{\max} , and self-supporting segment limit.

Robot Name	Image	n	m [kg]	l [mm]	τ_{\max} [N m]	n_{lim}
Uncle Sam [3]		8	0.32	101.60	1.30	2
SEA Snake [27]		8	0.41	128.00	7.00	5
Zmeelok-3M [28]		10	0.40	80.00	3.20	4
ACM-R5 [29]		9	0.80	170.00	9.00	3
Wheeko [30]		10	0.96	130.00	4.50	2

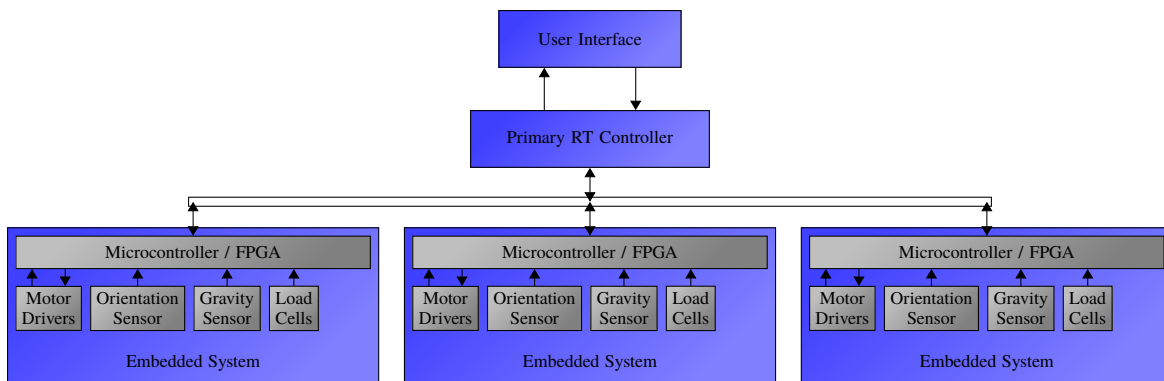


Fig. 17 Proposed system architecture for a future multi-segment system. Each segment has an embedded controller programmed with the cascaded control loop. The controller interfaces with the load cells for each TSA, the orientation sensors for the AUJ, an accelerometer to provide the local gravity vector for dynamics calculations, and the drivers for the TSA motors. A primary controller then uses a common control bus to interface with the embedded controllers, reading and writing data to registers to issue motion commands and get status updates.

6 Conclusion

This publication examines an existing prototype of an actuated universal joint with twisted string actuator to pinpoint enhancements and address limitations. Three key design improvements were identified and tested, resulting in an expanded AUJ angle range from $\pm 14.50^\circ$ to $\pm 26.00^\circ$, increased AUJ measurement accuracy from 0.21° to 0.11° , and zero recorded string failures under normal conditions. Additionally, the impact of added follower mass on AUJ performance was assessed to simulate multi-segment operation. Future efforts will focus on resolving remaining limitations, including installing load cells with larger full scales, developing a distributed control system for multi-segment operation, and exploring effective methods for measuring motor current under pulse width modulation (PWM) control or using brushless DC motors for accurate ATA assessment.

Acknowledgment

The lead author wishes to thank Dr. Dmitriy Makhnovskiy for his assistance in preliminary research for this publication.

Funding Data

- UKRI EPSRC Doctoral Training Partnership [1957210]
- UKRI Strength in Place Fund [84646 (AMPI)]

References

- [1] Rezaei, A., Shekofteh, Y., Kamrani, M., Fallah, A., and Barazandeh, F., 2008, "Design and control of a snake robot according to snake anatomy," *2008 International Conference on Computer and Communication Engineering*, IEEE, pp. 191–194.
- [2] Baba, T., Kameyama, Y., Kamegawa, T., and Gofuku, A., 2010, "A snake robot propelling inside of a pipe with helical rolling motion," *Proceedings of SICE Annual Conference 2010*, IEEE, pp. 2319–2325.

- [3] Wright, C., Buchan, A., Brown, B., Geist, J., Schwerin, M., Rollinson, D., Tesch, M., and Choset, H., 2012, "Design and architecture of the unified modular snake robot," *2012 IEEE international conference on robotics and automation*, IEEE, pp. 4347–4354.
- [4] Qin, G., Cheng, Y., Ji, A., Pan, H., Yang, Y., Yao, Z., and Song, Y., 2023, "Research on the cable-driven endoscopic manipulator for fusion reactors," *Nuclear Engineering and Technology*.
- [5] Würtz, T., May, C., Holz, B., Natale, C., Palli, G., and Melchiorri, C., 2010, "The twisted string actuation system: Modeling and control," *2010 IEEE/ASME International Conference on Advanced Intelligent Mechatronics*, pp. 1215–1220, doi: [10.1109/AIM.2010.5695720](https://doi.org/10.1109/AIM.2010.5695720).
- [6] Muehlbauer, P., Schimbera, M., Stewart, K., and Pott, P. P., 2021, "Twisted String Actuation for an Active Modular Hand Orthosis," *ACTUATOR; International Conference and Exhibition on New Actuator Systems and Applications 2021*, VDE, pp. 1–4.
- [7] Park, J., Park, J.-i., Seo, H.-T., Liu, Y., Kim, K.-S., and Kim, S., 2020, "Control of tendon-driven (Twisted-string Actuator) robotic joint with adaptive variable-radius pulley," *2020 20th International Conference on Control, Automation and Systems (ICCAS)*, IEEE, pp. 1096–1098.
- [8] Suthar, B. and Jung, S., 2021, "Design and Feasibility Analysis of a Foldable Robot Arm for Drones Using a Twisted String Actuator: FRAAD-TSA," *IEEE Robotics and Automation Letters*, **6**(3), pp. 5769–5775.
- [9] Palli, G., Natale, C., May, C., Melchiorri, C., and Wurtz, T., 2012, "Modeling and control of the twisted string actuation system," *IEEE/ASME Transactions on Mechatronics*, **18**(2), pp. 664–673.
- [10] Budynas, R. and Nisbett, J., 2011, *Shigley's Mechanical Engineering Design*, McGraw-Hill series in mechanical engineering, McGraw-Hill.
- [11] Nedelchev, S., Gaponov, I., and Ryu, J., 2020, "Accurate Dynamic Modeling of Twisted String Actuators Accounting for String Compliance and Friction," *IEEE Robotics and Automation Letters*, **5**(2), pp. 3438–3443.
- [12] Usman, M., Suthar, B., Seong, H., Hawkes, E., Gaponov, I., and Ryu, J.-H., 2017, "Passive returning mechanism for twisted string actuators," *2017 IEEE International Conference on Robotics and Automation (ICRA)*, IEEE, pp. 3714–3719.
- [13] Popov, D., Gaponov, I., and Ryu, J.-H., 2013, "Bidirectional elbow exoskeleton based on twisted-string actuators," *2013 IEEE/RSJ International Conference on Intelligent Robots and Systems*, IEEE, pp. 5853–5858.
- [14] Park, J., Kim, J. H., Kim, K.-S., and Kim, S., 2016, "Design and control of antagonistic robot joint with twisted string actuators," *2016 13th International Conference on Ubiquitous Robots and Ambient Intelligence (URAI)*, IEEE, pp. 563–565.
- [15] Lee, D., Kim, D. H., Che, C. H., In, J. B., and Shin, D., 2019, "Highly durable bidirectional joint with twisted string actuators and variable radius pulley," *IEEE/ASME Transactions on Mechatronics*, **25**(1), pp. 360–370.
- [16] Konda, R., Bombara, D., Chow, E., and Zhang, J., 2023, "Kinematic Modeling and Open-Loop Control of A Twisted String Actuator-Driven Soft Robotic Manipulator," *Journal of Mechanisms and Robotics*, pp. 1–18.
- [17] Crosby, D., Carrasco, J., Heath, W., and Weightman, A., 2022, "A Novel Triad Twisted String Actuator for Controlling a Two Degrees of Freedom Joint: Design and Experimental Validation," *2022 International Conference on Robotics and Automation (ICRA)*, IEEE, pp. 11388–11394.
- [18] Dessen, F., 1986, "Coordinating control of a two degrees of freedom universal joint structure driven by three servos," *Proceedings. 1986 IEEE International Conference on Robotics and Automation*, Vol. 3, pp. 817–822, doi: [10.1109/ROBOT.1986.1087559](https://doi.org/10.1109/ROBOT.1986.1087559).
- [19] Spong, M. W., Hutchinson, S., and Vidyasagar, M., 2020, *Robot modeling and control*, John Wiley & Sons.
- [20] Hillcrest Laboratories, Inc., 2017, *BNO080 Data Sheet*, 1st ed.
- [21] Guangdong Kingly Gear Co., 2020, *JL-J2FN20-50-06420*.
- [22] Dr. Fritz Fauhaber GmbH & Co. KG, 2020, *DC Micromotors - Precious Metal Commutation*.
- [23] Bienczyk, K., 2009, "Angle measurement using a miniature hall effect position sensor," *2009 2nd International Students Conference on Electrodynamic and Mechatronics*, IEEE, pp. 21–22.
- [24] Bourns, 2021, *PDB08 - 8 mm Micro Rotary Potentiometer*.
- [25] Dr. Fritz Fauhaber GmbH & Co. KG, 2018, *Motion Controllers - Series MCDC 3002 S*, 6th ed.
- [26] FUTEK Advanced Sensor Technology Inc., 2024, *LCM100 Miniature In Line Load Cell*.
- [27] Rollinson, D., Bilgen, Y., Brown, B., Enner, F., Ford, S., Layton, C., Rembisz, J., Schwerin, M., Willig, A., Velagapudi, P., et al., 2014, "Design and architecture of a series elastic snake robot," *2014 IEEE/RSJ International Conference on Intelligent Robots and Systems*, IEEE, pp. 4630–4636.
- [28] Varlashin, V. and Shmakov, O., 2019, "Comparative analysis of the virtual and physical experiments with a snake robot's rectilinear movement," *Journal of Physics: Conference Series*, Vol. 1326, IOP Publishing, Paper No. 1, p. 012037.
- [29] Yamada, H., 2005, "S. development of amphibious snake-like robot acm-r5," *The 36th international symposium on robotics (ISR 2005)*, Tokyo.
- [30] Liljeback, P., Pettersen, K. Y., Stavdahl, Ø., and Gravdahl, J. T., 2013, *Snake robots: modelling, mechatronics, and control*, Springer.

List of Figures

1	The value of θ_s increases the number of twists in a string bundle with a string length l_u	1
2	The location of r_s and optionally r_c in a string bundle.	2
3	Kinematic diagram of the antagonistic triad, where the universal joint rotation is defined by $\theta_{1,2}$ on the y and x axes respectively, and the actuator lengths are defined by $\lambda_{1,2,3}$ for the <i>top</i> , <i>left</i> and <i>right</i> strings, and r and $l_{1,2}$ define the anchor points of the strings.	2
4	Block diagram of the complete experimental control system, excluding the hardware velocity controllers for the motors. Dashed boxes correspond to the control layers $C_{1\dots 4}$	4
5	AUJ roll angle (θ_1) of the original prototype when the smallest TSA motor angle is equal to 2π , and motor angle of the “opposing” TSA (the TSA with the largest motor angle) at the same position.	4
6	An AUJ with a central universal joint, and one with a hollow spider. The hollow spider allows r to be decreased as space is no longer required for a central universal joint.	4
7	(a) The original TSA string loop between the string clamp and capstan bolt, with “pinch” and “bite” points indicated, where premature string failure may occur. (b) Section view of the new TSA string loop showing how the pinch and bite points have been eliminated.	5
(a)		5
(b)		5
8	Schematic of the latest prototype with labelled components.	5
9	Annotated photograph of the single segment physical prototype antagonistic triad, with the roll θ_1 and pitch θ_2 axes marked.	6
10	Plots of the response for three different trajectories, one on only the roll axis θ_1 (column 1), one on only the pitch axis θ_2 (column 2), and one on both axes θ_1 and θ_2 (column 3). Plots include AUJ orientation, forces at the top, left and right TSA, and the motor positions.	7
11	Comparison of the roll (θ_1) angle signal from the BNO080 IMU and PDB08 potentiometer when the AUJ is at rest at setpoint $\theta = [0 \ 0]$	8
12	AUJ roll tracking with increasing follower mass from table 5, plus with no mass at $k_p = 8000$ and $k_p = 8.00 \times 10^4$	8
13	Results of the trapezoidal velocity trajectory from table 6 for both AUJ pitch and roll trajectories, including the maximum absolute angle error for each cycle.	9
14	By adjusting f_{\min} , the transmission ratio of the TSA can be altered. Reducing f_{\min} increases the maximum TSA force f_{\max} while reducing the maximum TSA stroke velocity \dot{p}_{\max} . Conversely, increasing f_{\min} reduces f_{\max} and increases \dot{p}_{\max} . This can be used to actively modify the dynamic properties of the AUJ during operation. In this graph, $p = 0$	9
15	Sum of TSA maximum motor currents and angles for a simulated roll (θ_1) trajectory from figure 10 at different values of f_{\min} . Simulation uses motor coefficients from Faulhaber 1724TSR motors [22], as motor inertia and friction values are unavailable for Micro Metal Gearmotors.	10
16	Graph showing the decrease in self-supporting segments limit as TSA motor angle θ_s increases for different segment masses m at $p = 0$. Segment length is 155.00 mm measured from the prototype, other coefficients as used in figure 14 from table 2.	10
17	Proposed system architecture for a future multi-segment system. Each segment has an embedded controller programmed with the cascaded control loop. The controller interfaces with the load cells for each TSA, the orientation sensors for the AUJ, an accelerometer to provide the local gravity vector for dynamics calculations, and the drivers for the TSA motors. A primary controller then uses a common control bus to interface with the embedded controllers, reading and writing data to registers to issue motion commands and get status updates.	11

List of Tables

1	Table of the minimum and maximum values of $\Lambda(\theta)$ at different values of r in the interval of $[-\frac{\pi}{2}, \frac{\pi}{2}]$	3
2	Model coefficients for the latest prototype.	5
3	PID gains used for the experiment.	5
4	Summary of all the performance improvements and the measurements used to quantify them.	6
5	Table of all the follower mass configurations, with the parameters for follower mass m and follower COM z offset p_3	6
6	Trapezoidal trajectory sequence parameters.	6
7	List of snake robots, their number of segments n , their segment mass m , segment length l , maximum joint torque τ_{\max} , and self-supporting segment limit.	11